Distributed Brillouin scattering sensor for discrimination of wall-thinning defects in steel pipe under internal pressure

Lufan Zou, Graham A. Ferrier, Shahraam Afshar V., Qinrong Yu, Liang Chen, and Xiaoyi Bao

A distributed Brillouin scattering sensor has been employed to identify several inner wall cutouts in an end-capped steel pipe by measuring the axial and hoop strain distributions along the outer surface of the pipe. The locations of structural indentations that constitute 50–60% of the inner pipe wall are found and distinguished by use of their corresponding strain–pressure data. These results are quantified in terms of the fiber orientation, defect size and depth, and behavior relative to those of unperturbed pipe sections. © 2004 Optical Society of America

OCIS codes: 060.2370, 290.5830, 290.0290, 060.2310.

1. Introduction

Pipeline integrity and disturbance are generally not monitored because of a lack of reliable and durable techniques.[1] Pipeline disturbances such as cracking, corrosion, and tampering usually noticed only when the output flow is affected or when they have a severe effect on the surrounding environment. Unfortunately, the lack of information available on the types and locations of pipeline faults has created inefficient and potentially costly situations. For example, as a result of corrosion fatigue cracking, a 28-in. (71.12-cm-) diameter pipeline ruptured and released approximately 564,000 gallons of gasoline on 9 March 2000 in Greenville, Texas, which resulted in a damage-cleanup cost of $18,000,000.[2] In addition, corrosion was responsible for 63% of all pipeline failures in Canada from 1980 to 1997.[3] Although the Canadian pipeline industry spends more than $50,000,000 a year for inspection and maintenance, these pipeline failures occur with corresponding production losses and environmental cleanup and litigation costs. Hence there is an urgent need for a real-time structural-health monitoring system that can intelligently monitor the integrity of underground pipelines.

One of the major difficulties in monitoring pipelines stems from the fact that tens of meters to hundreds of kilometers of the pipeline length can be buried underground. Conventional conductive sensors have difficulties surviving their surrounding environments and have electrical noise problems. Furthermore, numerous such point-sensing devices are required for adequate monitoring of the health of long pipelines, and at a substantial cost. Fortunately, with the advent of optical fiber technology that uses low-cost optical fiber communication cables, distributed structural-health monitoring of pipelines can be achieved.

Fiber optic sensor technology has progressed at a rapid pace over the past decade. Many sensing techniques have been developed to monitor specific parameters.[1] In particular, distributed Brillouin scattering–based sensor systems provide an excellent opportunity for monitoring the structural health of civil structures[4] by allowing measurements to be taken along the entire length of the fiber, rather than only at discrete points, by use of the fiber itself as the sensing medium. One class of Brillouin-based sensor is based on the Brillouin loss technique[5] whereby two counterpropagating laser beams, a pulse and a cw, exchange energy through an induced acoustic field. When the beat frequency of the laser beams equals the acoustic (Brillouin) frequency v_B, the pulsed beam experiences maximum amplification from the cw beam. By measuring the depleted cw beam and scanning the beat frequency of the two

The authors are with the Fiber Optics Group, Department of Physics, University of Ottawa, 150 Louis Pasteur, Ottawa, Ontario K1N 6N5, Canada. L. Zou's e-mail address is lufan.zou@science.uottawa.ca.

Received 31 July 2003; revised manuscript received 10 November 2003; accepted 5 December 2003.

0003-6935/04/071583-06$15.00/0

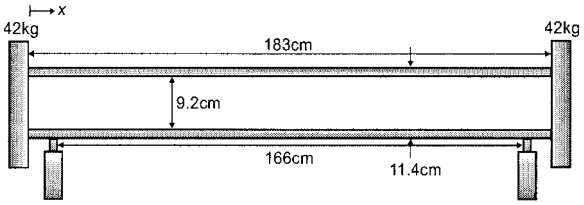

Fig. 1. Schematic diagram of the 1.83-m steel pipe used for the distributed Brillouin sensing experiment. The internal pressure was contained by two bolted 42 kg end caps, and a frame near each end supported the pipe.

lasers, one obtains a Brillouin loss spectrum centered about the Brillouin frequency. The sensing capability of Brillouin scattering arises from the dependence of Brillouin frequency v_B on the local acoustic velocity and refractive index in glass, which has a linear temperature and strain dependence[6,7]:

$$v_B(T_0, \varepsilon) = C_\varepsilon(\varepsilon - \varepsilon_0) + v_{B0}(T_0, \varepsilon_0), \quad (1)$$

$$v_B(T, \varepsilon_0) = C_T(T - T_0) + v_{B0}(T_0, \varepsilon_0), \quad (2)$$

where C_ε and C_T are the strain and temperature coefficients and ε_0 and T_0 are the strain and temperature that correspond to a reference Brillouin frequency v_{B0}. One obtains spatial information along the fiber length through optical time-domain analysis by measuring the propagation times for light pulses traveling in the fiber, thus allowing continuous temperature and strain distributions to be obtained.[4] This type of sensing has great potential for structural-health monitoring because one can adjust the spatial resolution for different applications simply by altering the pulse duration, even after the fiber is installed.

In this paper we report the results of our recent experiments in using a distributed Brillouin scattering sensor to detect pre-embedded inner-wall cutouts (defects) in an internally pressurized 1.83-m-long end-capped steel pipe. The pre-embedded defects, which constitute 50–60% of inner wall thickness, are discriminated by use of the corresponding strain measurements in the axial and hoop directions along the pipe.

2. Experimental Procedures

A. Preparation of Steel Pipe with Pre-Embedded Wall-Thinning Defects

To simulate the structural degradation of pipes we entrenched rectangular indentations within the inner wall of a steel pipe constructed at the Canmet Materials Technology Laboratory in Ottawa, Ontario, Canada, as shown in Fig. 1. The steel pipe was 1.83 m long, with two supporting points and a 42-kg end cap located at each of the two ends. The material specifications of the pipe are as follows: Poisson's ratio, 0.3; Young's modulus, 200 GPa (equal to 30×10^6 psi); length, 183 cm; outer diameter, 11.4 cm; wall thickness, 1.1 cm. The pipe was 90% filled with distilled water and pressurized with argon gas.

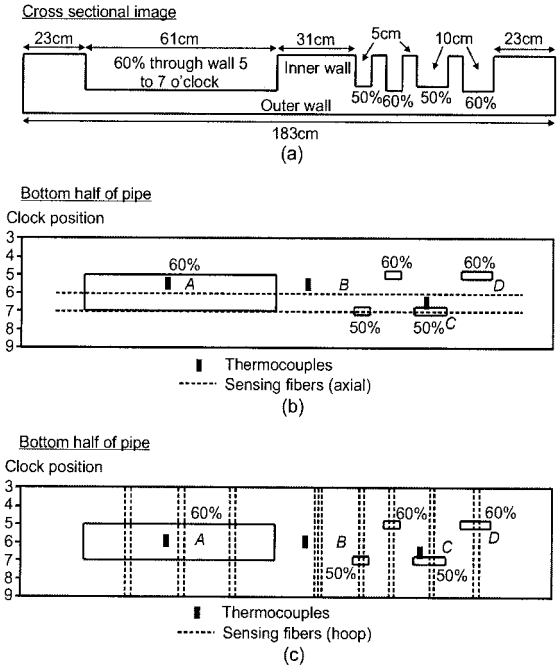

Fig. 2. Schematic diagram of the distribution of inner wall-cutouts (defects): (a) axial installation of sensing fiber (b) and hoop installation of sensing fiber (c). Region A is a 5.3 cm × 61 cm long cutout with 60% wall thinning, which starts at 23 and ends at 84 cm. Region B consists of the rest of the unperturbed pipe. Regions C and D are 1.3 cm × 10 cm cutouts with 50% and 60% wall thinning, respectively.

At predetermined locations along the pipe's inner wall, cutouts (defects) that constituted 50–60% of the wall thickness [as shown in Fig. 2(a)] were purposely implanted to simulate the condition in which a corroded pipeline has approached its threshold for replacement (compromise of 50% of the wall thickness). For comparison, we analyzed the behavior of a pipe with cutouts that constituted 60% of the wall thickness to determine whether the Brillouin sensor system could differentiate the strain responses of pipe regions that had different wall thicknesses. When a pipeline defect occurs, a certain percentage of the inner wall's thickness is lost, and larger strains appear in the defective region at a constant pressure within the pipe. The strain measurements were conducted at regular pressure intervals from 0 to 500 psi.

B. Installation of Sensing Fibers

A 30-m acrylate buffered SMF-28 optical fiber was used for monitoring both the environmental temperature conditions and the strain distributions along the pipe. The distribution of defects and sensing-fiber installations is shown in Fig. 2; the location and dimensions of cutouts A, C, and D are tabulated in Table 1; and region B constitutes the rest of the unperturbed pipe. To prepare the pipe for fiber installation we used sandpaper to remove irregularities caused by excess welding and provide a smooth, uniform surface about its circumference. We then pre-

Table 1. Parameters of Cutouts (Defects)

Cutout	Location (o'clock)	Reduced Thickness (%)	Width (cm)	Length (cm)
A	5–7	60	5.3	61
C	7	50	1.3	10
D	5	60	1.3	10

strained and mounted the optical fibers externally on the pipe to monitor the strain changes on the outer surface and secured them by using a special low-viscosity glue made by MasterCraft, which required approximately 3-h drying time. To prevent signal cross talk and additional noise that might result from fiber overlap we conducted the axial [Fig. 2(b)] and hoop [Fig. 2(c)] strain measurements separately. The temperature of the pipe was monitored by use of three thermocouples at various locations [Figs. 2(b) and 2(c)] and was found to have a negligible effect ($<\pm 5$ με) on strain measurements.

C. Distributed Brillouin Scattering Sensor System

The experimental setup for measurements of the Brillouin loss spectrum was reported previously.[8] The system is based on the interaction of a pulsed laser and a counterpropagating cw laser operating at a 1319-nm wavelength, as mentioned above. The pulsed beam is subjected to Brillouin amplification at the expense of the cw beam. The resultant power drops in the cw beam are measured while the frequency difference between two lasers is scanned, giving the Brillouin loss spectrum of the sensing fiber. The Brillouin shift of the fiber is determined from the spectrum and is used to evaluate the strain of the sensing fiber. We acquired Brillouin spectra every 5 cm (using a high-speed 2-GHz digitizer) along a 30-m fiber every half-hour by using 8000 waveform averages. Hence we used a pseudo-Voigt function[9] for peak fitting of each Brillouin spectrum to acquire frequency and strain information. Spatial resolution is determined by the pulse duration, which has a 1-to-1 correspondence with fiber position through $t = 2nd/c$, where d is the fiber position. For this experiment, a 1.3-ns pulse duration provided a 13-cm spatial resolution.

3. Results and Discussion

A. Measurement of Axial Strain

The axial strain was measured by use of the configuration shown in Fig. 2(b). Large defective region A ranges from 23 to 84 cm, and the remaining pipe is unperturbed along the 6-o'clock direction. The strain distribution along the longitudinal direction of the pipe under 200-psi internal pressure is presented in Fig. 3. The maximum (46-με) and minimum (14-με) strains occur in the middle of the defective and the unperturbed regions, respectively. As this 32-με difference is outside the experimental error range (~15 με based on a standard deviation) and therefore is caused directly by wall thinning, the capability of our system to distinguish defective and unperturbed regions is successfully demonstrated. In general, strains depend sensitively on proximity, end-cap size and type, and overall pipe design.[10] Because this steel pipe is asymmetric in terms of the distributions of defective regions, has a finite length with two 42-kg end caps, and is supported near both pipe ends (one is closed to the defective region; the other is at the unperturbed region), these complex boundaries produce complicated and different strain distributions near the boundaries at both sides of the pipe, i.e., strain decrease at the beginning of the big defective region A (~23 cm) and increase at the end of the unperturbed region (after 140 cm), as shown in Fig. 3. The compression that occurs at the beginning of defect A arises from the combination of the support point, the end cap, and 60% wall-thinning defect A. The increased tension that appears in the unperturbed region after 140 cm is related to the combination of the support point and the end cap that causes local stress risers.[10]

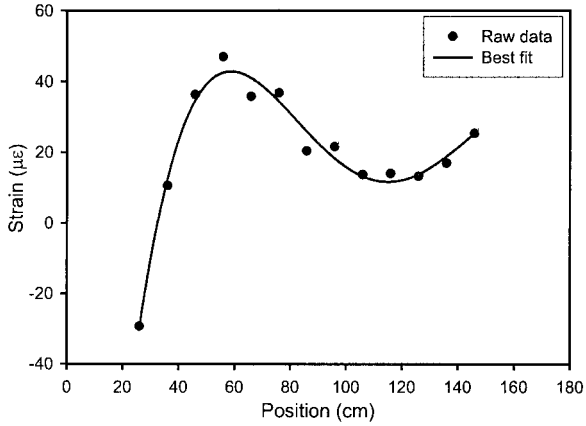

Fig. 3. Axial strain distribution along the longitudinal direction of the pipe through defect A and unperturbed region B. The strain difference between the maximum from the defective region and the minimum from the unperturbed region is 32 με at a 200-psi internal pressure.

The strain–pressure slopes of the defective region exceed those within the unperturbed region, as shown in Fig. 4. The strain–pressure slope obtains a maximum of 0.48 με/psi in the middle, which decreases toward the edges of the defect. However, a small local maximum arises near the edge between the defective and unperturbed regions located at 84 cm that is due to a noncontinuous boundary condition that results in a local stress concentration at the edge. In addition, reduced strain measurements near the defect boundary generally occur as a result of the overlapping 13-cm pulse, which acquires the average strain behavior from both regions and therefore leads to a strain–pressure ripple from 70 to 100 cm, as shown in Fig. 4. The strain–pressure slope remains constant at 0.16 με/psi within the experimental error near the middle of the unperturbed region, as expected, because the influence of boundaries is small there.

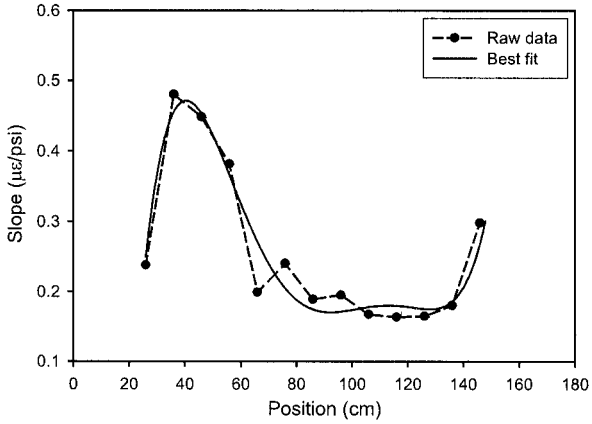

Fig. 4. Strain–pressure slope along the longitudinal direction of the pipe through defect A and unperturbed region B. The strain–pressure slope with 0.48 με/psi is highest in the defective region, decreases at the edges of the defect, and remains constant at 0.16 με/psi near the middle of the unperturbed region.

When a uniform pipe is operated within its elastic regime, its strain–pressure relationship remains linear. However, erosion or corrosion of the inner pipe wall causes irregular defective regions with reduced thickness. This increases their strain–pressure slopes relative to that of neighboring unperturbed regions, depending on defect size and thickness. Thus a bigger strain–pressure slope is observed for the middle of defect A (60% of inner-wall thickness) than for the middle of unperturbed region B and defect C (50% of inner-wall thickness), as shown in Fig. 5. The fact that the strain–pressure slope of region B is less than those of regions A and C demonstrates that pre-embedded defects that consist of 50% and 60% of the reduced inner-wall thickness can be discriminated from the corresponding axial strain measurements.

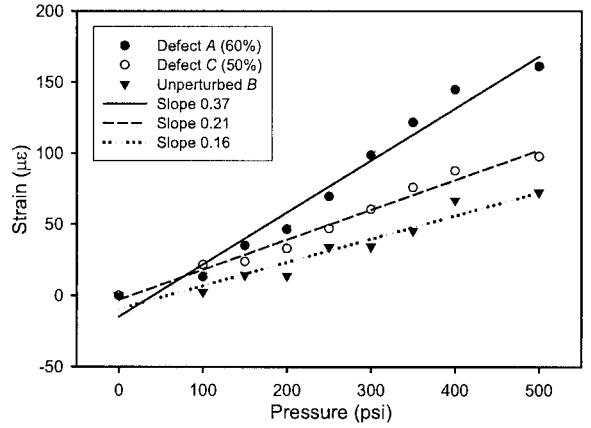

Fig. 5. Axial strain–pressure slopes of defects A, C, and D. A bigger strain–pressure slope is shown for the middle of defect A (60%-depleted wall) compared with the middle of unperturbed region B and defect C (50%-depleted wall).

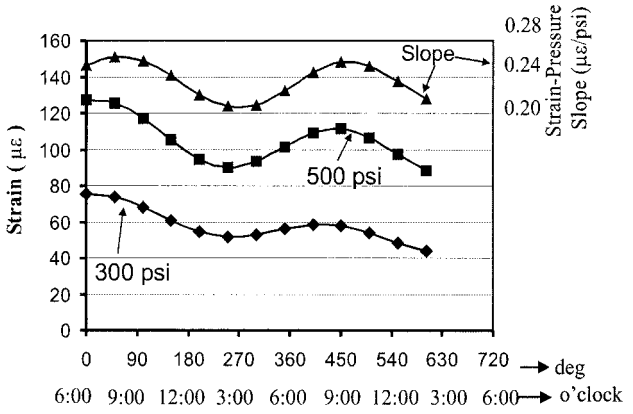

Fig. 6. Hoop strain distributions about one pipe circumference encompassing defective region A. Two maxima, corresponding to one complete loop, can be observed.

B. Measurement of Hoop Strain

Distributed hoop strain measurements were obtained with the fiber configuration shown in Fig. 2(c). The widths of defects A, C, and D are 5.3, 1.3, and 1.3 cm, respectively. As the spatial resolution of our measurement is 13 cm, there is a signal overlap between the unperturbed and the defective regions even in the middle of the defects along the circumferential direction. However, we can still differentiate the hoop strain measurements of the locations close to and far from the middle of the defects, even for small defects C and D.

Typical strain distributions about one pipe circumference that encompasses defective region A are displayed in Fig. 6. Two maxima, which correspond to one complete loop, have been observed in the hoop strain and strain–pressure slope distribution of the defective region under 300- and 500-psi internal pressures. The differences between the maximum, which corresponds to the defective region, and the minimum, which corresponds to the unperturbed region, are ~20 and ~40 με under internal pressures of 300 and 500 psi, respectively, which are outside the experimental error range (~15 με of the standard deviation) and therefore are definitely caused by wall thinning. The strain maxima and highest strain–pressure slopes are observed approximately once every 360°.

We chose two points, one in the defective region (6-o'clock position) and the other in the unperturbed region (12-o'clock position); Fig. 7 shows a linear strain–pressure relationship for these two points with slopes of 0.27 and 0.21 με/psi, respectively. As the minimum and maximum slopes of 0.21 and 0.27 με/psi are spaced approximately 180° apart (as shown in Fig. 6), the defective and unperturbed regions are clearly differentiated.

To compare defective regions that have the same arc length but different penetration depths we measured their strain–pressure slopes directly, to see the effects of wall penetration. As shown in Fig. 8, the strain–pressure slopes of defective regions C and D

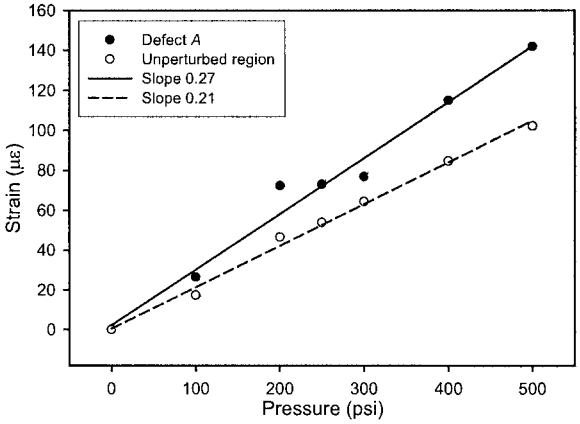

Fig. 7. Strain–pressure slopes about one pipe circumference encompassing defective region A obtained by hoop strain measurements. The minimum and maximum slopes of 0.21 and 0.27 με/psi, spaced approximately 180° apart, correspond to the unperturbed and defective regions, respectively.

are 0.18 and 0.21 με/psi, which correspond to 50%- and 60%-depleted walls, respectively. As expected, a larger strain–pressure slope indicates a thinner pipe wall. The unperturbed wall in both fiber loops experiences a constant strain–pressure slope of 0.15 με/psi.

The hoop strain results can also be used to distinguish among defective regions at different locations along the pipe. One can achieve this by determining the average of all strain–pressure slopes about a single fiber loop and comparing it with other averages along the pipe. The average of all strain–pressure slopes obtained about one fiber loop is a good indication of the arc length of the defective region. Hence the average strain slopes of 0.24 and 0.18 με/psi for fiber loops wrapping defective regions A and D indicate the dominance of a larger defective region A (5.3 cm wide) over the smaller region D (1.3 cm wide) for equal depth (60% of inner-wall thickness) on the net strain distribution about one fiber loop.

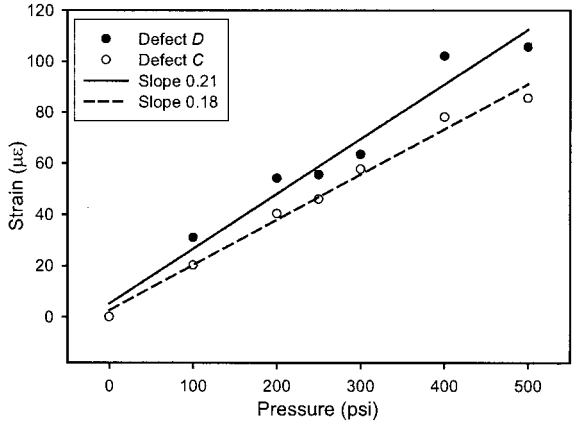

Fig. 8. Strain–pressure slopes obtained by hoop strain measurements of defects C and D. The strain–pressure slopes of defective regions C and D are 0.18 and 0.21 με/psi, corresponding to 50- and 60%-depleted walls, respectively. As expected, a larger strain–pressure slope indicates a thinner pipe wall.

Certainly, the location near the middle of the defects experiences the maximum slope, and the minimum slope happens at locations farthest from the middle of the defects, i.e., the unperturbed region (12-o'clock position) because the deformations of defective regions are larger than those of unperturbed regions. The strain–pressure slope increases with defect width and depth, which indicates that preembedded large or small defects that constitute 50–60% of the inner wall thickness can be discriminated by hoop strain measurements. Because defects C and D are very small (1.3 cm wide), though they have different wall thicknesses they do not affect the neighboring unperturbed regions significantly. Thus the corresponding unperturbed regions (12-o'clock positions) maintain a 0.15-με/psi strain–pressure slope. The higher strain–pressure slope from the unperturbed (12-o'clock) region opposite the large defect A (0.21 με/psi) is likely due to the bigger deformation of the large defect.

4. Conclusions

We have demonstrated the capability of a distributed Brillouin scattering sensor system to identify several inner-wall cutouts in an end-capped steel pipe by measuring the axial and hoop strain distributions along the outer surface of the pipe. For the axial strain measurement, maximum and minimum strains that correspond to the middle of defective and unperturbed regions have been measured; thus the capability of our system to differentiate between these two regions has been demonstrated. Maximum and minimum strains, which correspond to defective and unperturbed regions, respectively, have also been observed in the hoop strain distribution of one complete loop. This demonstrates the ability of our system to differentiate between defective and unperturbed regions about the circumference of the pipe. By measuring hoop strain–pressure slopes at different points along the pipe we have also been able to discriminate among defective regions of different sizes and thickness. Thus, various-sized preembedded defects that compose 50–60% of the inner-wall thickness can be discriminated by both axial and hoop measurements. Our results show that fiber optic sensor technology based on distributed Brillouin scattering offers great potential as a figurative nervous system for infrastructure elements that allow high-performance, cost-effective health and damage assessment systems to be achieved.

This research was supported in part by Intelligent Sensing of Innovative Structures, Canada. The authors thank S. Papavinasam and A. Doiron of Canmet Materials Technology Laboratory in Ottawa, Ontario, Canada for providing the steel pipe and associated help, and G. Shen of Canmet Materials Technology Laboratory for useful discussions.

References

1. E. Tapanes, "Fibre optic sensing solutions for real-time pipeline integrity monitoring," presented at the Australian Pipeline Industry Association National Convention, 27–30 October 2001; http://www.iceweb.com.au/Newtech/FFT_Pipeline_Integrity_Paper.pdf.
2. National Transportation Safety Board, "Pipeline accident brief" (National Transportation Safety Board, Washington, D.C., 2001); http://www.ntsb.gov/publictn/2001/PAB0103.htm.
3. Energy and Utilities Board, "Pipeline performance in Alberta 1980–1997" (Energy and Utilities Board, Calgary, Alberta, Canada, 1998); http://www.eub.gov.ab.ca/bbs/documents/reports/r98g.pdf.
4. X. Bao, M. DeMerchant, A. Brown, and T. Bremmer, "Tensile and compressive strain measurement in the lab and field with the distributed Brillouin scattering sensor," J. Lightwave Technol. **19,** 1698–1704 (2001).
5. X. Bao, D. J. Webb, and D. A. Jackson, "32-km distributed temperature sensor based on Brillouin loss in an optical fiber," Opt. Lett. **18,** 1561–1563 (1993).
6. T. Horiguchi, T. Kurashima, and M. Tateda, "Tensile strain dependence of Brillouin frequency shift in silica optical fibers," IEEE Photon. Technol. Lett. **1,** 107–108 (1989).
7. T. Kurashima, T. Horiguchi, and M. Tateda, "Thermal effects on Brillouin frequency shift in jacketed optical silica fibers," Appl. Opt. **29,** 2219–2222 (1990).
8. X. Zeng, X. Bao, C. Y. Chhoa, T. W. Bremner, A. W. Brown, M. D. DeMerchant, G. Ferrier, A. L. Kalamkarov, and A. V. Georgiades, "Strain measurement in a concrete beam by use of the Brillouin-scattering-based distributed fiber sensor with single-mode fibers embedded in glass fiber reinforced polymer rods and bonded to steel reinforcing bars," Appl. Opt. **41,** 5105–5114 (2002).
9. A. W. Brown, M. D. DeMerchant, X. Bao, and T. W. Bremner, "Spatial resolution enhancement of a Brillouin distributed sensor using a novel signal processing method," J. Lightwave Technol. **17,** 1179–1183 (1999).
10. D. Heckman, "Finite element analysis of pressure vessels" (Monterey Bay Aquarium Research Institute, Moss Landing, Calif. 1998), http://www.mbari.org/education/internship/98interns/98internpapers/98heckman.pdf.